The Role of Mesoscale Tracer Transports in the Global Ocean Circulation

Gokhan Danabasoglu; James C. McWilliams; Peter R. Gent

Science, New Series, Vol. 264, No. 5162 (May 20, 1994), 1123-1126.

Stable URL:
http://links.jstor.org/sici?sici=0036-8075%2819940520%293%3A264%3A5162%3C1123%3ATROMTT%3E2.0.CO%3B2-1

Science is currently published by American Association for the Advancement of Science.

Your use of the JSTOR archive indicates your acceptance of JSTOR's Terms and Conditions of Use, available at http://www.jstor.org/about/terms.html. JSTOR's Terms and Conditions of Use provides, in part, that unless you have obtained prior permission, you may not download an entire issue of a journal or multiple copies of articles, and you may use content in the JSTOR archive only for your personal, non-commercial use.

Please contact the publisher regarding any further use of this work. Publisher contact information may be obtained at http://www.jstor.org/journals/aaas.html.

Each copy of any part of a JSTOR transmission must contain the same copyright notice that appears on the screen or printed page of such transmission.

JSTOR is an independent not-for-profit organization dedicated to creating and preserving a digital archive of scholarly journals. For more information regarding JSTOR, please contact support@jstor.org.

http://www.jstor.org/
Fri Dec 17 17:31:58 2004

turbulent eddy diffusivity varies spatially and that the deviations are linked to variations of the internal wave field. The canonical internal wave field in the deep ocean interior appears to support only weak diapycnal mixing ($K_\rho \sim K_T \sim 0.1 \times 10^{-4}$ m^2 s^{-1}). Large dissipation rates (supporting diffusivities much greater than 1×10^{-4} m^2 s^{-1}) seem possible in areas where the intensity of the internal wave field is enhanced. One such region is near the bottom where wave reflection, wave generation, or both can effectively perturb the background wave field. We believe the central question to be as follows: Can boundary processes alone account for the spatially averaged eddy diffusivity of 1×10^{-4} m^2 s^{-1} or more that is derived by large-scale analyses (*2*)? Given an interior diffusivity of order 0.1×10^{-4} m^2 s^{-1}, hypsographic considerations (*25*) would seem to require large boundary diffusivities: perhaps 10×10^{-4} to 100×10^{-4} m^2 s^{-1}. Alternatively, bottom generation might cause the internal wave field to be generally enhanced at depth, which in turn would result in enhanced mixing. More extensive observations of microstructure and fine structure in the deep ocean and improved theories of internal wave generation and reflection at boundaries are needed.

REFERENCES AND NOTES

1. K. Wyrtki, *Deep-Sea Res.* **8**, 39 (1961).
2. W. H. Munk, *ibid.* **13**, 707 (1966).
3. N. G. Hogg, P. Biscaye, W. Gardner, W. J. Schmitz, *J. Mar. Res.* **40** (suppl.), 231 (1982).
4. A. E. Gargett, *ibid.* **42**, 359 (1984); M. C. Gregg, *J. Geophys. Res.* **92**, 5249 (1987); *J. Phys. Oceanogr.* **7**, 436 (1977).
5. J. N. Moum and T. R. Osborn, *J. Phys. Oceanogr.* **16**, 1250 (1986).
6. R. W. Schmitt *et al.*, *J. Atmos. Oceanic Technol.* **5**, 484 (1988).
7. The spectrum of the ocean internal wave field commonly exhibits universal characteristics, first described in mathematical form by C. Garrett and W. Munk [*Geophys. Fluid Dyn.* **3**, 225 (1972)]. This construct has been refined with time and the collection of additional data. We interpret our observations with reference to the spectrum presented by C. Garrett and W. Munk [*J. Geophys. Res.* **80**, 291 (1975)], as modified by J. L. Cairns and G. O. Williams [*ibid.* **81**, 1943 (1976)]. The shorthand notation for this description is GM76.
8. J. R. Ledwell, A. J. Watson, C. S. Law, *Nature* **364**, 701 (1993).
9. Turbulent scale velocity gradients were sampled with air-foil shear probes [T. R. Osborn, *J. Phys. Oceanogr.* **4**, 109 (1974)] calibrated at the Bedford Institute of Oceanography facility operated by N. Oakey. One-half–meter segments of velocity-gradient data were Fourier transformed and integrated to obtain estimates of shear variance. The integration was extended to a minimum in spectral energy density (beyond which the spectra were dominated by noise). The dissipation rates were derived on the assumption that the flow field was isotropic. Fast-response glass-bead thermistors (FP-07) were used to sample temperature microstructure; temperature gradient variance was also estimated in frequency space as outlined above, and the dissipation rate was derived on the assumption of isotropy. A thermistor calibration was constructed for each profile with data from a platinum resistance thermometer on the HRP, which in turn was calibrated in the Woods Hole Oceanographic Institution facility. Data from both microstructure sensors were corrected for probe and electronic interface responses before the estimation of the variance [K. L. Polzin, thesis, Woods Hole Oceanographic Institution/Massachusetts Institute of Technology Joint Program (1992)].
10. P. Nasmyth, thesis, Institute of Oceanography, University of British Columbia (1970).
11. N. S. Oakey, *J. Phys. Oceanogr.* **12**, 256 (1982). Consistency of the K_T and K_ρ estimates reported in Table 1 suggest that $\Gamma = 0.25$ is, on average, a reasonable value. Taking a smaller value for Γ exacerbates the discrepancy between the indirect and microstructure-based estimates of the diapycnal diffusivity.
12. G. K. Batchelor, *J. Fluid Mech.* **5**, 113 (1959).
13. T. R. Osborn and C. S. Cox, *Geophys. Fluid Dyn.* **3**, 321 (1972).
14. T. R. Osborn, *J. Phys. Oceanogr.* **10**, 83 (1980).
15. The bootstrap method we used to derive uncertainty estimates followed the work of B. Efron and G. Gong [*Am. Stat.* **37**, 36 (1983)]. Dissipation profiles were depth-averaged over 10 m {yielding, according to run tests [M. C. Gregg, H. E. Sein, D. B. Percival, *J. Phys. Oceanogr.* **23**, 1777 (1993)], roughly independent samples} and binned into 200-m intervals. The binned populations were repeatedly subsampled and averaged. The error bars shown for each depth segment in Fig 2 represent the 3rd and 97th percentile of the distribution of 100 mean estimates formed by the random sampling of one-half of the available data in each bin. These confidence intervals are not substantially different from the 95% confidence intervals based on an assumed log-normal distribution [M. A. Baker and C. H. Gibson, *ibid.* **17**, 1817 (1987)]. A similar procedure beginning with dissipation estimates normalized by vertical density and temperature gradients (computed over 20- to 50-m scales) yielded the error bars for diffusivity in Fig. 3 and Table 1. In consideration of the relatively small sample sizes, this error metric may not represent the true uncertainty, particularly for the deep NATRE data that exhibited a meridional trend. The trend manifested itself as larger error bars for the average dissipation and diffusivity values for the Atlantic experiment than those for the Pacific.
16. J. M. Toole, E. Kunze, K. L. Polzin, R. W. Schmitt, *Eos* **75** (suppl.), 164 (1994).
17. F. S. Henyey, J. Wright, S. M. Flatte, *J. Geophys. Res.* **91**, 8487 (1986); F. S. Henyey, "Proceedings of 'Aha Huliko'a Hawaiian Winter Workshop," University of Hawaii at Manoa, 13 to 18 January 1991, *Sch. Ocean Earth Sci. Technol. Spec. Publ.* (1991), pp. 233–236; M. C. Gregg, *J. Geophys. Res.* **94**, 9686 (1989).
18. K. L. Polzin, J. M. Toole, R. W. Schmitt, unpublished data.
19. Linear wave theory provides a measure of average wave frequency from the ratio of buoyancy-scaled shear variance to strain variance [E. Kunze, A. J. Williams III, M. G. Briscoe, *J. Geophys. Res.* **95**, 18127 (1990)]. The terms in this ratio are estimated here by the respective integration of velocity and isopycnal displacement-gradient wave-number spectra to the fine-scale cutoff in the shear spectra (*18*).
20. O. M. Phillips, *The Dynamics of the Upper Ocean* (Cambridge Univ. Press, New York, ed. 2, 1977); C. C. Eriksen, *J. Geophys. Res.* **15**, 1145 (1985).
21. T. H. Bell, *J. Geophys. Res.* **80**, 320 (1975).
22. G. Siedler and U. Paul, *ibid.* **96**, 22259 (1991).
23. P. Saunders, *J. Phys. Oceanogr.* **13**, 1416 (1983).
24. M. G. Briscoe and R. A. Weller, *Dyn. Atmos. Oceans* **8**, 243 (1984).
25. L. Armi, *J. Geophys. Res.* **83**, 1971 (1978).

26. We thank the officers and crew of the R/V *New Horizon* and R/V *Oceanus*; E. Montgomery, R. Koehler, M. Cook, and D. Wellwood for technical support; and N. Oakey for advice and encouragement. Supported by the Office of Naval Research through grants (N00014-89-J-1073 and N00014-92-J-1323) to the Woods Hole Oceanographic Institution and by the National Science Foundation.

27 December 1993; accepted 31 March 1994

The Role of Mesoscale Tracer Transports in the Global Ocean Circulation

Gokhan Danabasoglu,* James C. McWilliams, Peter R. Gent

Ocean models routinely used in simulations of the Earth's climate do not resolve mesoscale eddies because of the immense computational cost. A new parameterization of the effects of these eddies has been implemented in a widely used model. A comparison of its solution with that of the conventional parameterization shows significant improvements in the global temperature distribution, the poleward and surface heat fluxes, and the locations of deep-water formation.

The oceans play important roles in regulating the Earth's climate and must be included when the effects of increasing greenhouse gases such as CO_2 are assessed. Sea-surface temperature largely dictates the heat flux between the atmosphere and ocean. The salinity of the upper ocean is also important in determining where deep-water formation occurs by convection. This deep-water formation drives the global thermohaline circulation, sometimes called the ocean conveyor belt (*1*), which controls the horizontal transports of heat and fresh water and the absorption of increasing CO_2 in the atmosphere.

The most energetic oceanic motions occur on the mesoscale, with length scales of 10 to 100 km. The ubiquitous mesoscale eddies are important in the transports of heat, salt, and passive tracers such as radiocarbon and freon in all parts of the world's oceans. Their importance has been documented from observations in the Antarctic Circumpolar Current (ACC) (*2*) and the

National Center for Atmospheric Research, Boulder, CO 80307, USA.

*To whom correspondence should be addressed.

equatorial Pacific (3) and North Atlantic (4) oceans.

If an ocean model is to resolve the mesoscale explicitly, then its horizontal resolution must be on the order of 10 km. Ocean climate modeling also requires good vertical resolution and integrations of thousands of years so that the deep ocean is near equilibrium. For the short term, eddy-resolving global ocean models cannot be used routinely in climate simulations, even on modern supercomputers. Thus, there is a pressing need for a parameterization of mesoscale eddies for climate studies.

The most widely used ocean model is that developed at the Geophysical Fluid Dynamics Laboratory (GFDL) in the 1960s (5). The early practice was to assume that the effect of eddies is a down-gradient diffusion of momentum and tracers in the horizontal and vertical directions with constant diffusion coefficients. The results from this model are sensitive to these coefficients; for example, no single value of the vertical diffusivity gives both a poleward heat transport and a main thermocline sharpness that agree with observations (6). More recently, the practice has been to use diffusivities that vary with depth (7, 8).

However, the use of horizontal tracer diffusion conflicts with well-established observations that tracers are more uniformly distributed along surfaces of constant potential density (isopycnals) than along horizontal surfaces (9). In particular, in regions where isopycnals slope steeply, horizontal diffusion implies tracer fluxes across isopycnals that can be a hundred times the cross-isopycnal fluxes estimated from ocean microstructure observations (10). Thus, a proposal was made (11) that horizontal and vertical diffusion in the tracer equation should be replaced by diffusion along and across isopycnals. An approximation to this form of diffusion, based on small isopycnal slopes, was implemented in the GFDL model (12). However, in practice it has been found that this proposal is computationally unstable when the cross-isopycnal coefficient is kept small, as required by observations; some horizontal tracer diffusion is necessary for numerical stability. However, even a small horizontal diffusivity can have globally detrimental effects on the solutions because density slopes are steep in strong currents (13). The reason for the instability is that isopycnal diffusion has no effect on the density distribution and, hence, on the large-scale ocean circulation. Thus, tracer diffusion along isopycnals is an incomplete parameterization of the effects of mesoscale eddies.

The dynamical balance in equilibrium is between the mean advection and the eddy transport of tracers. This equilibrium balance can be obtained if the dynamical effect

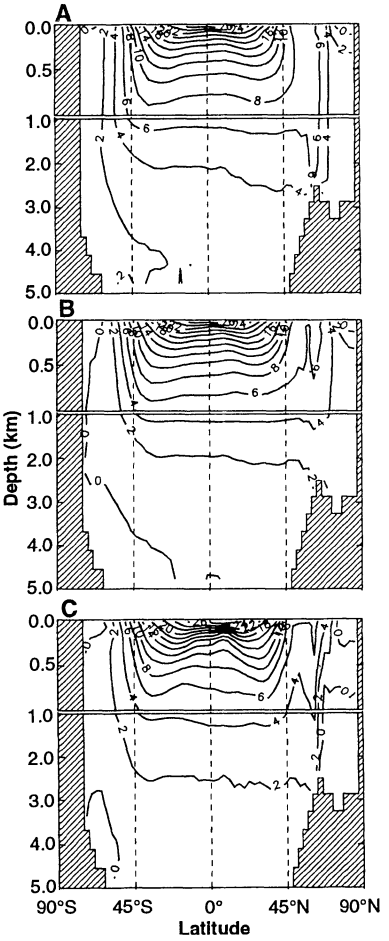

Fig. 1. Time and zonal mean potential temperature, θ: (**A**) with HOR, (**B**) with ISO, and (**C**) from climatology (17). Contour interval = 2°C.

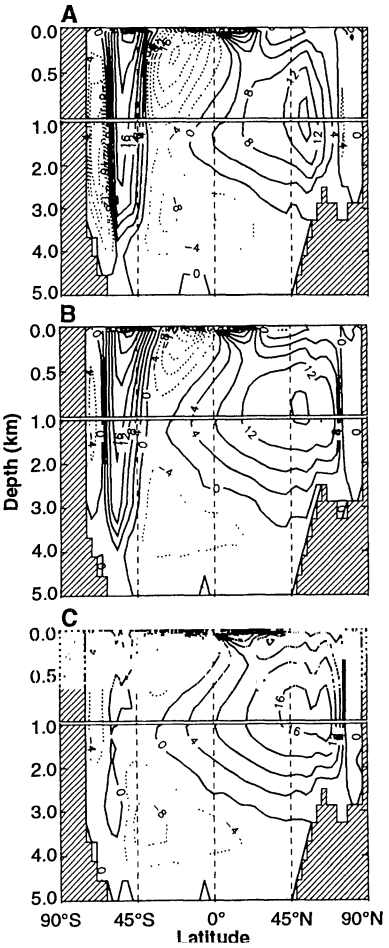

Fig. 2. Time and zonal mean meridional overturning stream function: (**A**) mean velocity with HOR, (**B**) mean velocity, and (**C**) effective transport velocity with ISO. Contour interval = 4 Sv.

of eddies is parameterized as an adiabatic, down-gradient diffusion of the thickness between neighboring isopycnal surfaces (14), in addition to the diffusion of tracers along isopycnals (11). This parameterization depletes large-scale potential energy by mimicking eddy generation by the instability of ocean currents, an energy pathway that is otherwise absent in adiabatic, non-eddy-resolving models. The additional parameterization component can be expressed entirely in terms of an additional tracer advection (15). Thus, this component has an effect like that often discussed in the context of stratospheric tracer distributions, in which the mean tracer is advected by the "effective transport velocity," that is, the sum of the mean velocity plus the eddy-induced transport velocity (16). Because this velocity is nondivergent and has zero boundary flux, it gives several adiabatic conservation principles: for example, all integral moments of density (14). Buoyancy-forced calculations require a vertical (cross-isopycnal) diffusion that has a small coefficient, κ_V, except where the fluid is gravitationally unstable and convection occurs. We refer to this parameterization suite as ISO, and its tracer equation for potential temperature θ is

$$\left[\frac{\partial}{\partial t} + (\mathbf{u} + \mathbf{u}^*)\cdot\nabla + (w + w^*)\frac{\partial}{\partial z}\right]\theta = R(\kappa_I, \theta) + (\kappa_V \theta_z)_z \quad (1)$$

where t is time, ∇ is the horizontal gradient operator, z is the vertical direction, and R is diffusion along isopycnals with coefficient κ_I. Advection in Eq. 1 is by the effective transport velocity, which is the sum of the mean velocity $(\mathbf{u},w)$ and the eddy-induced transport velocity $(\mathbf{u}^*,w^*)$. The latter is defined by

$$\mathbf{u}^* = (\kappa_I \nabla\rho/\rho_z)_z,\ w^* = -\nabla\cdot(\kappa_I \nabla\rho/\rho_z) \quad (2)$$

where ρ is the potential density. We can compare ISO to the conventionally parameterized tracer equation designated HOR, which is

$$\left[\frac{\partial}{\partial t} + \mathbf{u}\cdot\nabla + w\frac{\partial}{\partial z}\right]\theta = \nabla\cdot(\kappa_H \nabla\theta) + (\kappa_V \theta_z)_z \quad (3)$$

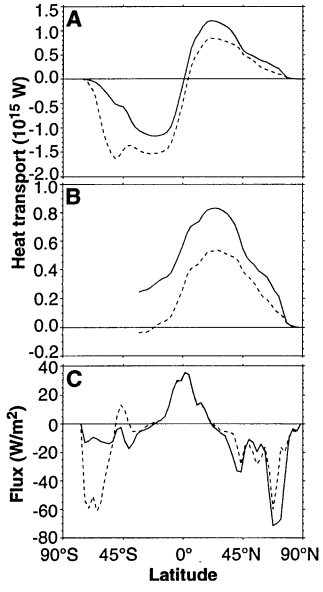

Fig. 3. (**A** and **B**) Mean northward heat transport (A) in all oceans and (B) in the Atlantic. (**C**) Surface heat flux in all oceans. For (A) to (C): ISO, solid trace; HOR, dotted trace.

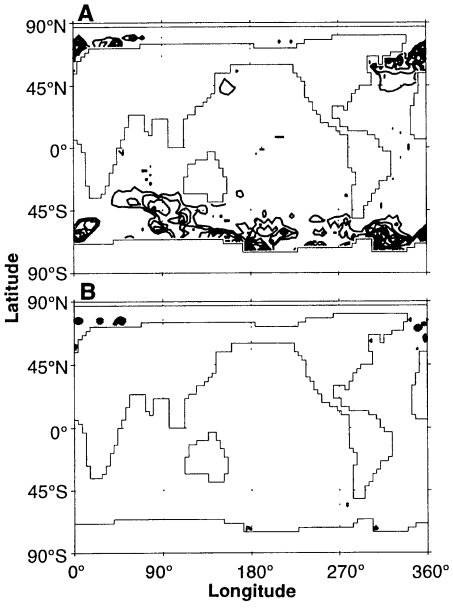

Fig. 4. The percentage of all times and levels when convection occurs (**A**) with HOR and (**B**) with ISO. Contour interval = 5%.

where κ_H is the horizontal diffusivity. The model is completed with analogous equations for additional tracers (including salinity), expressions for momentum and mass balance, and the equation of state for sea water (*5*).

We now compare two solutions that are equivalent, except that one uses ISO and the other HOR. The posing is conventional for the global general circulation. Momentum boundary conditions are no normal velocity at all boundaries, no slip at the side boundaries, specified wind stress from the European Centre for Medium-Range Weather Forecasting at the top boundary, and a quadratic drag law at the bottom boundary. The tracer boundary conditions are relaxation to climatology (*17*) at the top boundary with a time constant of 30 days and insulation at all other boundaries. The forcing fields have the time mean and the annual and semiannual cycles. The model resolution is 4° in longitude, 3° in latitude, and 20 levels in the vertical, monotonically increasing from 50 m near the top to 450 m near the bottom. The values of the viscosities and diffusivities used in the two solutions are $\nu_V = 2 \times 10^{-3}$, $\nu_H = 10^6$, $\kappa_V = 5 \times 10^{-5}$, $\kappa_H = 2 \times 10^3$, and $\kappa_I = 10^3$ m^2 s^{-1}, which are within the usual ranges for this resolution. The solutions have been integrated for 10,000 years to an annually repeating equilibrium state.

Latitude and depth sections of mean potential temperature for all oceans are shown in Fig. 1. With HOR (Fig. 1A), almost the entire ocean is warmer than observed (Fig. 1C) by more than 2°C around 1000 m but decreasing to about 1°C in the deep ocean. This result indicates that the main thermocline in Fig. 1A is weaker (more diffuse) than it is in the ocean because the upper boundary condition ensures that the surface θ is close to the observed values. These two model errors are known to be chronic in the GFDL model (*5*). With ISO (Fig. 1B), however, the thermocline is sharper, although not quite so much as it is in climatological measurements (Fig. 1C). In the deep ocean, the warm bias has been reversed with ISO, resulting in a distinct improvement in the global θ distribution. An integral measure is the globally averaged potential temperature, 5.2°, 3.3°, and 3.6°C in HOR, ISO, and climatology, respectively.

The zonally averaged overturning circulation is represented by the meridional stream function. The stream function calculated with HOR (Fig. 2A) shows shallow, wind-driven cells of upwelling at the equator, with most of the water sinking within 20°; Northern Hemisphere sinking at high latitudes and a return flow mostly before the equator, with a maximum transport of 17 sverdrups (Sv; 1 Sv = 10^6 m^3 s^{-1}) centered at 54°N and 1000 m; and a strong dipole circulation in the ACC between 40°S and Antarctica, with transports of −18 and 17 Sv in the two cells (the equatorward of these cells is often called the Deacon cell). In contrast, with ISO (Fig. 2B) the tropical cells are somewhat shallower; the northern thermohaline circulation extends much farther to the south with an increase of nearly 5 Sv through the subtropics; and the Deacon cell in Fig. 2B is very similar to that in Fig. 2A, but its poleward companion shows much less deep-water formation.

With ISO, the tracer advection in Eq. 1 is by the effective transport velocity (not just the mean velocity), so we also examine its meridional overturning stream function (Fig. 2C). This stream function shows a dramatic change in the Southern Hemisphere: The Deacon cell is totally absent. Thus, in the ACC the zonally integrated, eddy-induced transport velocity is almost exactly equal and opposite to the zonally integrated mean velocity. This behavior is reminiscent of atmospheric jets in which eddy effects can almost compensate for the effects of the mean flow (*16*). Because of the great contrast between Figs. 2A and 2C, we can anticipate a dramatic change in tracer distributions, such as radiocarbon (*8*). Also in Fig. 2C, the tropical circulation reaches farther south to 45°S, and the Northern Hemisphere circulation increases its strength somewhat (to 18 Sv) and reaches deeper within the Southern Hemisphere. Because the eddy-induced transport velocities are small in the Northern Hemisphere, the big improvement in its overturning circulation is primarily due to the absence of horizontal diffusion in ISO; a similar effect was found in a higher resolution model of the Atlantic Ocean (*13*). The large eddy-induced velocities in the ACC have also been shown in diagnostic calculations with climatology (*15*).

The northward heat transport in all oceans is plotted in Fig. 3A. With HOR, the maximum transport in the Southern Hemisphere is 1.6 PW (10^{15} watts) at 51°S, with the greater part due to horizontal diffusion. The location of this extremum does not agree with empirical estimates (*18*). This error is removed with ISO, whose maximum transport in the Southern Hemisphere is 1.2 PW at 21°S, and it is nearly all due to mean advection. The largest contribution to the transport by the eddy-induced transport velocity is 0.4 PW at 45°S, which is close to the estimate from climatology (*15*). The surface heat flux (equal to the derivative of the meridional heat flux) shows a dramatic drop with ISO within and poleward of the ACC (Fig. 3C), and its reduced value is consistent with empirical estimates (*19*); this drop is a consequence of the diminished Deacon cell (Fig. 2C). The heat transport with ISO is more symmetric about the equator, as observed in (*18*). In the Northern Hemisphere, the poleward flux is considerably enhanced with ISO, where the maximum increases to 1.2 PW, compared to 0.8 PW with HOR. Nearly all of the increased transport occurs in the Atlantic Ocean (Fig. 3B), where the maximum northward transport is greater than 0.8 PW at 24°N with ISO; this transport distribution is a consequence of the broader overturning

circulation with ISO (Fig. 2C). In a high-resolution Atlantic model, the maximum northward heat transport with ISO is 1 PW (*13*). Thus, in both models with ISO there is consistency with the empirical estimate at 25°N of 1.1 ± 0.3 PW (*20*), which does not occur with HOR.

With HOR, convection occurs in many places (Fig. 4A), much more extensively than is thought to occur in nature. In the ACC, the reason for this difference is the extensive upwelling near 60°S (Fig. 2A) that weakens the density stratification and conduces convection. This upwelling is much weaker with ISO (Fig. 2C), and there is consequently much less convection there (Fig. 4B). In general, with ISO deep-water formation occurs only in a few small locations: in the Arctic and far North Atlantic, in the Labrador Sea, and in the Weddell and Ross seas around Antarctica where deep-water formation has been observed.

A new, isopycnally oriented, adiabatic parameterization for mesoscale tracer transport has been tested in a non-eddy–resolving, global ocean model. This parameterization replaces the physically unjustifiable horizontal diffusion that has been the common practice, and it produces substantial improvements: a sharper main thermocline, a cooler abyssal ocean, a meridionally expanded overturning circulation in the North Atlantic that strengthens the poleward and surface heat fluxes, an eddy-induced cancellation of the Deacon cell that greatly diminishes the poleward and surface heat fluxes across the ACC, and a confinement of deep convection to regions where it is known to occur.

REFERENCES

1. W. S. Broecker, *Oceanography* **4**, 79 (1991).
2. H. L. Bryden, *J. Mar. Res.* **37**, 1 (1979); R. A. de Szoeke and M. D. Levine, *Deep Sea Res.* **28**, 1057 (1981).
3. H. L. Bryden and E. C. Brady, *J. Mar. Res.* **47**, 55 (1989).
4. J. C. McWilliams *et al.*, in *Eddies in Marine Science*, A. R. Robinson, Ed. (Springer-Verlag, Berlin, 1983), pp. 92–113.
5. K. Bryan and M. D. Cox, *Tellus* **19**, 54 (1967); *J. Atmos. Sci.* **25**, 945 (1968).
6. F. Bryan, *J. Phys. Oceanogr.* **17**, 970 (1987).
7. K. Bryan and L. J. Lewis, *J. Geophys. Res.* **84**, 2503 (1979).
8. J. R. Toggweiler, K. Dixon, K. Bryan, *ibid.* **94**, 8217 (1989).
9. C. O'D. Iselin, *Eos* **20**, 414 (1939); R. B. Montgomery, *Bull. Am. Meteorol. Soc.* **21**, 87 (1940).
10. T. J. McDougall and J. A. Church, *J. Phys. Oceanogr.* **16**, 196 (1986); M. C. Gregg, *J. Geophys. Res.* **92**, 5249 (1987).
11. M. H. Redi, *J. Phys. Oceanogr.* **12**, 1154 (1982).
12. M. D. Cox, *Ocean Modelling* **74**, 1 (1987).
13. C. Boning, W. R. Holland, F. Bryan, G. Danabasoglu, J C. McWilliams, unpublished results.
14. P. R. Gent and J. C. McWilliams, *J. Phys. Oceanogr.* **20**, 150 (1990).
15. P. R. Gent, J. Willebrand, T. J. McDougall, J. C. McWilliams, unpublished results.
16. D. G. Andrews, J. R. Holton, C. B. Leovy, *Middle Atmosphere Dynamics* (Academic Press, Orlando, FL, 1987); R. A. Plumb and J. D Mahlman, *J. Atmos. Sci.* **44**, 298 (1987).
17. S. Levitus, *Nat. Oceanic Atmos. Adm. Prof. Pap. 13* (1982), p. 1.
18. K. Trenberth and A. Solomon, *Clim. Dyn.*, in press.
19. A. L. Gordon and H. W. Taylor, in *Numerical Models of Ocean Circulation* (National Academy of Sciences, Washington, DC, 1975), pp. 54–56.
20. H. L. Bryden and M. M. Hall, *Science* **207**, 884 (1980).

28 December 1993; accepted 4 March 1994

Rules for α-Helix Termination by Glycine

Rajeev Aurora, Rajgopal Srinivasan, George D. Rose*

A predictive rule for protein folding is presented that involves two recurrent glycine-based motifs that cap the carboxyl termini of α helices. In proteins, helices that terminated in glycine residues were found predominantly in one of these two motifs. These glycine structures had a characteristic pattern of polar and apolar residues. Visual inspection of known helical sequences was sufficient to distinguish the two motifs from each other and from internal glycines that fail to terminate helices. These glycine motifs—in which the local sequence selects between available structures—represent an example of a stereochemical rule for protein folding.

The folded structure of a protein is encrypted in its amino acid sequence (*1*), written in a code that remains obscure. Is this fold the inevitable outcome of an energetically controlled process, like rolling a ball down a hill? Or do discrete instructions for each structural motif reside somewhere in the sequence? Such alternatives cannot be distinguished by the observation of a folding reaction, any more than a computer algorithm can be deduced by the observation of the way a running program transforms input to output. We have been exploring the hypothesis that protein conformation is specified by a stereochemical code (*2*), similar in principle to the code for DNA, in which strand complementarity is determined by hydrogen bonds (*3*). Focusing initially on the α helix, we analyzed proteins of known structure to extract patterns and modeled short fragments to characterize each pattern fully.

The α helix is characterized by consecutive main chain hydrogen bonds between each amide hydrogen and the carbonyl oxygen of the previous helical turn (*4*). This pattern is truncated at helix ends because, upon termination, no next turn of the helix exists to provide hydrogen bond partners. Such end effects are substantial, encompassing two-thirds of the residues for the helix of average length (*5*). The term helix "capping" is used to describe those alternative hydrogen bond patterns that can satisfy the backbone N–H and C=O groups in the initial and final turns of the helix, respectively (*5, 6*). Capping stabilizes α helices in both proteins (*7–9*) and peptides (*7, 10–12*) and inhibits expected fraying (*10, 13*).

In this report we describe and analyze two Gly-based capping motifs that are prevalent at the COOH-termini of α helices. From the analysis, a set of simple stereochemical rules was developed. With these rules, the visual inspection of known helical sequences was sufficient to differentiate between the two motifs and distinguish them from internal Gly residues that did not terminate helices.

The nomenclature for helices and their flanking residues is as follows:

. . . –N″–N′–Ncap–N1–N2–N3– . . .

. . .–C3–C2–C1–Ccap–C′–C″– . . .

where N1 through C1 belong to the helix proper and the primed residues belong to turns that bracket the helix at either end. Ncap and Ccap are boundary residues that belong to both the helix and the adjacent turn. In practice, residues classified as helical have backbone dihedral angles, ϕ and ψ, with mean values of $-64° \pm 7°$ and $-41° \pm 7°$, respectively; Ncap and Ccap make one additional intrahelical hydrogen bond while departing from these means (*5*).

All capping interactions were cataloged among the α helices of 42 proteins of known structure (*14*). Consistent with earlier findings (*5*), the NH_2-termini of helices were capped predominantly by nearby residue side chains. In contrast, the COOH-termini were usually capped by local backbone interactions, many involving Gly residues.

Approximately one-third of all α helices terminate with a Gly residue at the COOH-terminus. Helices terminating in Gly can be classified by their hydrogen bonding pattern into two primary motifs (Fig. 1). The larger class, which includes 24 of the

Department of Biochemistry and Molecular Biophysics, Washington University School of Medicine, St. Louis, MO 63110, USA.

*To whom correspondence should be addressed.